






Real-space and reciprocal-space topology in the $\text{Eu}(\text{Ga}_{1-x}\text{Al}_x)_4$ square net system

Jaime M. Moya ^{1,2,3}, Jianwei Huang ^{2,3}, Shiming Lei,^{2,3} Kevin Allen ^{2,3}, Yuxiang Gao,^{2,3} Yan Sun,⁴ Ming Yi ^{2,3} and E. Morosan ^{2,3,*}

¹*Applied Physics Graduate Program, Rice University, Houston, Texas 77005, USA*

²*Department of Physics and Astronomy, Rice University, Houston, Texas 77005, USA*

³*Rice Center for Quantum Materials (RCQM), Rice University, Houston, Texas 77005, USA*

⁴*Shenyang National Laboratory for Materials Science, Institute of Metal Research, Chinese Academy of Sciences, Shenyang, Liaoning 110016, China*



(Received 6 February 2023; revised 29 June 2023; accepted 3 August 2023; published 31 August 2023)

Magnetotransport measurements of the centrosymmetric square net $\text{Eu}(\text{Ga}_{1-x}\text{Al}_x)_4$ compounds reveal evidence of both reciprocal- and real-space topology. For compositions $0.50 \leq x \leq 0.90$, several intermediate field phases are found by magnetization measurements when $H \parallel c$, where a maximum in the topological Hall effect is observed, pointing to the existence of topological (real-space topology) or noncoplanar spin textures. For $0.25 \leq x \leq 0.39$, magnetization measurements reveal an intermediate field state, but no transition is visible in the Hall measurements. For $x = 0.15$, only one magnetic transition occurs below the Néel temperature T_N , and no intermediate field spin reorientations are observed. The Hall effect varies smoothly before the spin-polarized (SP) state. However, in the SP state, Hall measurements reveal a large anomalous Hall effect (AHE) for all compositions, a consequence of reciprocal-space topology. Density functional theory calculations in the paramagnetic state indeed reveal a Dirac point that lies very near the Fermi energy, which is expected to split into Weyl nodes in the SP state, thereby explaining the observed AHE. These results suggest the $\text{Eu}(\text{Ga}_{1-x}\text{Al}_x)_4$ family is a rare material platform where real- and reciprocal-space topology exist in a single material platform.

DOI: [10.1103/PhysRevB.108.064436](https://doi.org/10.1103/PhysRevB.108.064436)

I. INTRODUCTION

The advent of topological materials has generated much interest not only from a fundamental physics perspective, but also due to their potential applications in revolutionary electronic devices. For example, the theoretical prediction of the quantum anomalous Hall effect (QAHE) [1,2], a consequence of Berry curvature [3] in reciprocal space, promises the possibility of quantized, chiral, dissipation-free electron transport without magnetic fields, ideal for energy efficient electronic devices. The reality of such a device was brought one step closer with the experimental realization of the QAHE in the topological insulator Cr-doped $\text{Bi}(\text{Sb})_2\text{Te}_3$ [4].

The notions of topology in condensed matter systems also extend to real space via topological spin textures which are particle-like, noncoplanar spin configurations characterized by a topological charge [5]. Topological spin textures have been proposed for applications in next-generation memory, logic, spintronic, and neuromorphic computing devices [6–10]. Furthermore, itinerant electrons coupled to topological spin textures acquire Berry phase when traversing the noncoplanar spin textures. Therefore, the topological spin textures can be regarded as real-space sources of Berry curvature, resulting in the topological Hall effect (THE) [5].

Combining reciprocal- and real-space topology extends the phase space of approaches for future spintronic applications. For example, proof-of-principle experiments based on topological insulator/magnetic heterostructures exhibit both the

THE and QAHE: this approach takes advantage of the THE to read out the spin-state information, which, in turn, can be transmitted without dissipation using the QAHE chiral edge states [11–16]. Compared to their heterostructure counterparts, bulk magnetic topological materials offer the chance for stronger coupling between magnetism and itinerant electrons. However, the concurrence of reciprocal- and real-space topology has not yet been observed in a bulk system.

The $\text{Eu}(\text{Ga}_{1-x}\text{Al}_x)_4$ series can be considered an ideal platform for such reciprocal- and real-space topology coexistence. $\text{Eu}(\text{Ga}_{1-x}\text{Al}_x)_4$ crystallizes in the tetragonal space group $I4/mmm$ [17] with the crystal structure composed of square nets of Eu atoms separated by Al/Ga layers, also with square net motifs [18]. The square net features of the Al/Ga metalloid layer provide a natural platform for Weyl physics [18], as well as enhanced nesting conditions for incommensurate magnetism [19].

The $x = 0$ compound EuGa_4 orders magnetically into a simple A -type antiferromagnetic (AFM) structure [20]. No intermediate phases are observed below the Néel temperature in the magnetic field–temperature (H - T) phase diagram [18]. However, above T_N , angle-resolved photoemission spectroscopy (ARPES) data show the existence of fourfold-degenerate spinless nodal rings (NRs) near the Fermi level in EuGa_4 [18]. With the application of a magnetic field $H \parallel c$, when the magnetization is saturated in the spin-polarized (SP) state, the spin degeneracy is lifted, and two topological Weyl NRs are realized, protected by mirror symmetry [18]. The topological NRs, whose signatures are observed in magnetotransport measurements [18], are responsible for the large quantum mobility and large, unsaturated

*em11@rice.edu

magnetoresistance reaching a value of 200 000% at $\mu_0 H = 14$ T and $T = 2$ K [18,21]. The $x = 1$ compound, EuAl_4 , [17,22–26] has a complex H - T phase diagram with several spin reorientation transitions for $H \parallel c$ [22–24]. A nonzero THE in select regions of the H - T phase diagram led to the proposal of topological spin textures in EuAl_4 [23]. Later, the existence of a skyrmion lattice was confirmed via small-angle neutron scattering measurements [22]. The evidence of the reciprocal-space topology in EuGa_4 and real-space topology in EuAl_4 prompts the search for the coexistence of the two types of topological states across the $\text{Eu}(\text{Ga}_{1-x}\text{Al}_x)_4$ series.

The $\text{Eu}(\text{Ga}_{1-x}\text{Al}_x)_4$ crystal structure has two crystallographic sites for Al or Ga to occupy [17]. For $x = 0.5$, the Al and Ga preferentially occupy the two different sites, leading to an ordered structure of EuGa_2Al_2 [17]. EuGa_2Al_2 has also been shown to have a complex H - T phase diagram for $H \parallel c$, with a nonzero THE maximum centered around an intermediate field phase, pointing to the existence of either a topological spin texture or another noncoplanar spin texture [27]. The exact nature of this intermediate field state is yet to be determined.

The existence of reciprocal- and real-space topology for the two end members EuGa_4 and EuAl_4 , respectively, and the persistence of the THE in EuGa_2Al_2 , motivate a detailed study on the $\text{Eu}(\text{Ga}_{1-x}\text{Al}_x)_4$ series, with a goal of identifying compositions where both topological phenomena might coexist. To this end, $\text{Eu}(\text{Ga}_{1-x}\text{Al}_x)_4$ single crystals with $x = 0.15, 0.24, 0.31, 0.39, 0.50, 0.58, 0.71$, and 0.90 were synthesized. In the magnetically ordered state, the THE for $x \geq 0.50$ with $H \parallel c$ is observed, pointing to the existence of topological or, more generally, noncoplanar spin textures. Additionally, a large intrinsic AHE is registered in the field-induced spin-polarized (SP) state when the magnetization is saturated for compositions $0.24 \leq x \leq 0.71$, suggesting reciprocal-space band topology. Density functional theory (DFT) calculations indicate the existence of a Dirac point near the Fermi energy in EuGa_2Al_2 . The Dirac point is expected to split into Weyl nodes in the SP state, responsible for the large AHE in $\text{Eu}(\text{Ga}_{1-x}\text{Al}_x)_4$.

II. EXPERIMENTAL METHODS

Single crystals of $\text{Eu}(\text{Ga}_{1-x}\text{Al}_x)_4$ were synthesized using a self-flux method described in Ref. [17]. Powder x-ray diffraction measurements were collected with a Bruker D8 Advance diffractometer with Cu K_α radiation. Rietveld refinements were done using FullProf software [28] and the obtained lattice parameters are consistent with the previous results [17]. Quantitative elemental analysis by wavelength dispersive spectrometry (WDS) of $\text{Eu}(\text{Ga}_{1-x}\text{Al}_x)_4$ phase was performed using the EPMA (Electron Probe Micro-Analyzer) instrument at Rice University, with a JEOL JXA 8530F Hyperprobe equipped with a field emission (Schottky) emitter and five WDS spectrometers. The analytical conditions used were 15 kV accelerating voltage, 20 nA beam current, and a spot beam size of ~ 300 nm. The standards used for composition calibration were synthetic in-house produced stoichiometric compounds EuGa_4 and EuAl_4 . Careful background offsets were manually selected for each element to avoid interferences with higher-order x-rays during peak and

background measurement. Each element (Ga, Al, and Eu) was simultaneously analyzed on two spectrometers, in order to improve the statistics on the standard deviation and detection limit calculation for each measurement. The reproducibility of the standards was accurate and precise, with an error below 1% for each element. ZAF matrix correction was employed for quantification.

Magnetization measurements were done using a Quantum Design Dynacool system equipped with a vibrating sample magnetometer. Four-probe resistivity measurements were made using the electrical transport option in the same system with the typical applied current $j = 5$ mA and frequency $f = 9.15$ Hz. Measurements of the longitudinal resistivity as a function of magnetic field H , $\rho_{xx}(H)$, and Hall measurements, $\rho_{yx}(H)$, were measured in a complete field-sweep loop with four quadrants: quadrant I from $H > 0$ to $H = 0$, quadrant II from $H = 0$ to $H < 0$, quadrant III from $H < 0$ to $H = 0$, and quadrant IV from $H = 0$ to $H > 0$. The subsequent measurements were symmetrized or antisymmetrized, respectively. No hysteresis was observed for any composition.

The electronic band structure was calculated based on density functional theory by using the code of the Vienna *Ab initio* Simulation Package (VASP) [29] with projected augmented wave potential. The exchange and correlation energies were considered at the level of the generalized gradient approximation, following the Perdew-Burke-Ernzerhof parametrization scheme [30]. The energy cutoff was set as 500 eV. The calculations have dealt with f electrons as the valance states. To calculate the surface state, we projected the Bloch wave functions into maximally localized Wannier functions (MLWFs) [31] derived from the $\text{Eu-}5d$, $\text{Eu-}6s$, $\text{Eu-}6p$, $\text{Ga-}4s$, $\text{Ga-}4p$, $\text{Al-}3s$, and $\text{Al-}3p$ orbitals. The tight-binding model Hamiltonian was constructed from the MLWF overlap matrix. Based on the tight-binding Hamiltonian, the surface state was considered under open boundary conditions with the half-infinite two-dimensional model using the iterative Green's function method [32,33].

III. RESULTS AND DISCUSSION

Hall effect measurements have proven a powerful tool to identify systems with large sources of Berry curvature $\mathbf{\Omega}_k$ [5,23,34–49]. Systems with nonzero $\mathbf{\Omega}_k$ have an additional term in the Hall conductivity σ_{xy} besides the normal-metal component, and this is the anomalous Hall conductivity σ_{xy}^A that depends on $\mathbf{\Omega}_k$ as $\sigma_{xy}^A = -(e^2/h) \int d^3k \Omega_k^z / (2\pi)^3$ [48]. Berry curvature can either be generated via the Karplus-Luttinger-type (KL) mechanism [50], first discussed in the context of ferromagnets, or the scalar spin chirality (SSC) [51–53] mechanism. In the former, spin-orbit coupling has always been emphasized as a key ingredient while the derivation of the quantum Hall conductivity by Thouless *et al.* [54] and subsequent interpretation of the nonquantized anomalous Hall conductivity by Haldane [55] made clear the relationship between reciprocal-space topology and the anomalous Hall effect. In the latter, when the SSC defined as $\chi_{ijk} = \mathbf{S}_i \cdot (\mathbf{S}_j \times \mathbf{S}_k)$ (where $\mathbf{S}_{i,j,k}$ are the spins of three adjacent sites in a lattice) is nonzero, the real-space noncoplanar spin textures act as sources of Berry curvature. In the literature the Hall response contributed from the SSC-type mechanism is often

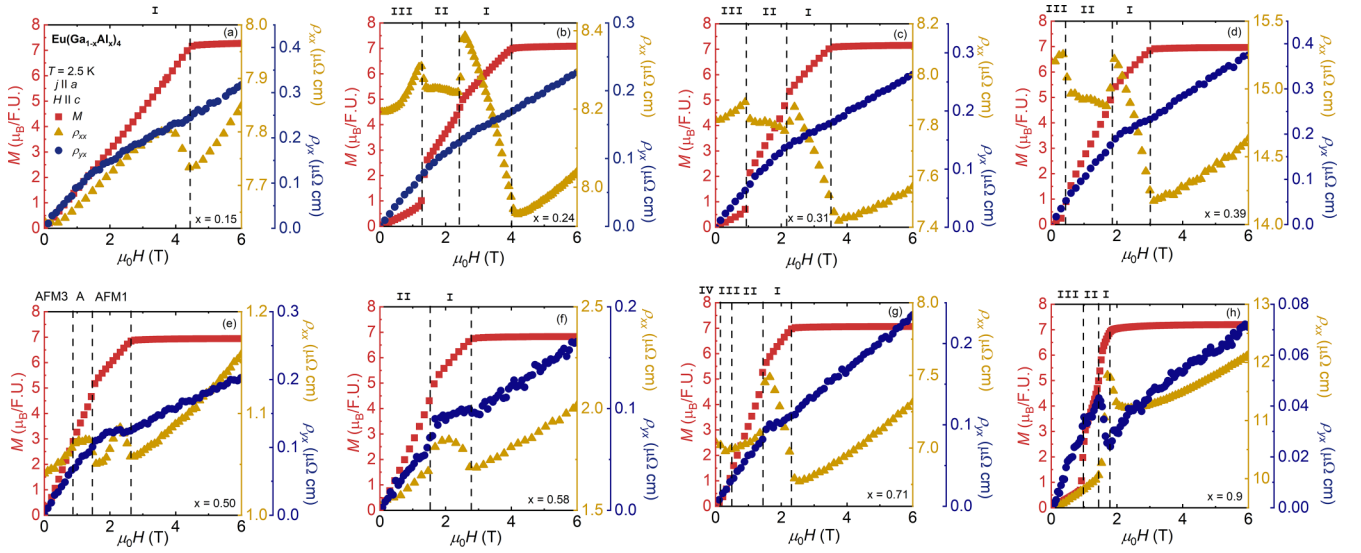


FIG. 1. Magnetization M (red squares, left axis), resistivity ρ_{xx} (gold triangles, inner right axis), and Hall resistivity ρ_{yx} (blue circles, outer right axis) as a function of magnetic field $\mu_0 H$ measured with magnetic field $H \parallel c$ at temperature $T = 2.5$ K for $\text{Eu}(\text{Ga}_{1-x}\text{Al}_x)_4$, (a) $x = 0.15$, (b) $x = 0.24$, (c) $x = 0.31$, (d) $x = 0.39$, (e) $x = 0.50$, (f) $x = 0.58$, (g) $x = 0.71$, and (h) $x = 0.90$. The transport measurements are measured with the current $j \parallel a$. Phase boundaries are marked with a dashed line.

referred to as the topological Hall effect. Since topological spin textures are noncoplanar, they should therefore exhibit a topological Hall effect if they are metallic [5,39,56].

A. Topological Hall effect

Since both types of Hall effects are related to the magnetic properties, field-dependent magnetization data M for $\text{Eu}(\text{Ga}_{1-x}\text{Al}_x)_4$ (blue squares, Fig. 1) are compared with resistivity measurements ρ_{xx} (gold triangles) and Hall resistivity ρ_{yx} (blue circles), measured at $T = 2.5$ K $< T_N$, with $H \parallel c$, and current $j \parallel a$. Signatures of field-induced spin reorientation are clearly observed by anomalies in both M and ρ_{xx} , which are marked by the vertical dashed lines in Fig. 1. Qualitatively, the behavior of ρ_{yx} below the fields $\mu_0 H_c$ where M saturates can be grouped into two categories depending on composition, as discussed below.

For $0.15 \leq x \leq 0.39$ [Figs. 1(a)–1(d)], ρ_{yx} is concave down below H_c with no obvious discontinuities even though there are clear magnetic transition features in both M and ρ_{xx} curves. For $x = 0.15$ [Fig. 1(a)], only one magnetic phase transition is observed, which is similar to the behavior of the end compound EuGa_4 , where the field induces a magnetic transition from the AFM ground state to the fully SP state [57]. It is therefore unlikely for this composition to host topological spin textures. For $0.24 \leq x \leq 0.39$ [Figs. 1(b)–1(d)], the magnetic field drives the system through multiple magnetic phases, which are clearly captured in M and ρ_{xx} , but not very evident in the ρ_{yx} curves. The concave down feature in ρ_{yx} for $0.15 \leq x \leq 0.39$ [Figs. 1(a)–1(d)] is similar to that observed in GdPtBi [35]. In theory, a band-structure-induced anomalous Hall contribution that does not scale with M is possible for certain noncollinear spin textures that break time-reversal and lattice symmetries of a simple antiferromagnetic state [35,58]. Future experiments to resolve the magnetic spin textures together with theoretical analysis will be insightful

to understand the ρ_{yx} in the magnetically ordered state for compositions $0.15 \leq x \leq 0.39$.

For $0.50 \leq x \leq 0.90$ [Figs. 1(e)–1(h)], ρ_{yx} shows discontinuities corresponding to some of the magnetic transitions that are also revealed in M and ρ_{xx} . The discontinuity in ρ_{yx} suggests the existence of the THE, which is observed in many well-established skyrmion-hosting materials, such as MnSi [47,59], Gd_2PdSi_3 [39], $\text{Gd}_3\text{Ru}_4\text{Al}_2$ [56], and GdRu_2Si_2 [60]. Such a discontinuity is associated with the first-order nature of the field-induced magnetic transition. Therefore it is concluded that the $\text{Eu}(\text{Ga}_{1-x}\text{Al}_x)_4$ compounds with $0.5 \leq x \leq 0.90$ are promising candidates to host real-space topological spin textures. Next the THE for these compositions is evaluated. The measured Hall resistivity ρ_{yx} for a metallic magnet can have multiple contributions:

$$\rho_{yx} = R_0 \mu_0 H + \rho_{yx}^A + \Delta \rho_{yx}. \quad (1)$$

Here, the first term $R_0 \mu_0 H$ is the normal Hall resistivity arising from the Lorentz force the charge carriers experience as they traverse a perpendicular magnetic field $\mu_0 H$, where R_0 is the Hall coefficient. When the system has one dominant carrier, the normal Hall effect is typically linear in field.

The second term ρ_{yx}^A is the anomalous Hall resistivity which scales with M . ρ_{yx}^A can also have multiple contributions; however, depending on the magnitude of the conductivity $\sigma_{xx} = \rho_{xx}/(\rho_{xx}^2 + \rho_{yx}^2)$, one contribution usually dominates. Empirically, for highly conductive systems, i.e., $\sigma_{xx} > 10^6$ ($\Omega \text{ cm}$) $^{-1}$, the anomalous Hall conductivity $\sigma_{yx}^A = \rho_{yx}^A/(\rho_{xx}^2 + \rho_{yx}^2)$ is dominated by skew scattering and varies linearly with σ_{xx} [48]. Assuming $\rho_{yx} \ll \rho_{xx}$, $\rho_{yx}^A = S_H M \rho_{xx}$, when skew scattering dominates, where S_H is the anomalous Hall coefficient.

The so-called intrinsic regime, where the AHE is dominated by the KL mechanism [50], is empirically found to be in the range 10^4 ($\Omega \text{ cm}$) $^{-1} < \sigma_{xx} < 10^6$ ($\Omega \text{ cm}$) $^{-1}$ [48]. In this

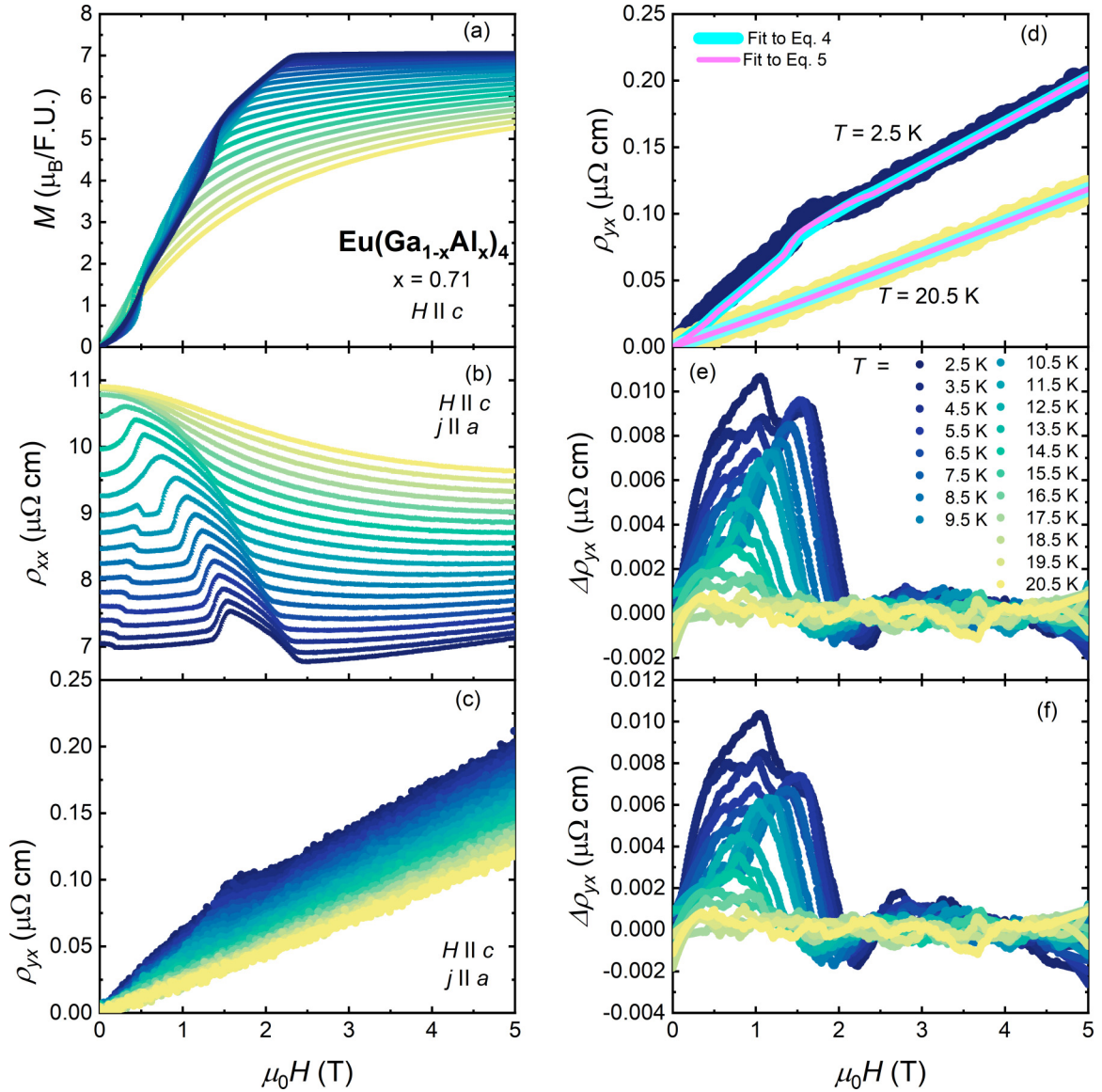


FIG. 2. Topological Hall effect for $\text{Eu}(\text{Ga}_{1-x}\text{Al}_x)_4$ with $x = 0.71$. (a) Isothermal magnetization M , (b) longitudinal resistivity ρ_{xx} , and (c) Hall resistivity ρ_{yx} measured as a function of magnetic field μ_0H with field $H \parallel c$ at temperatures $2.5 \text{ K} \leq T \leq 20.5 \text{ K}$. Transport measurements are measured with current $j \parallel a$. (d) ρ_{yx} at $T = 2.5 \text{ K}$ (blue circles) and $T = 20.5 \text{ K}$ (yellow circles) with fits to Eq. (4) (cyan lines) and Eq. (5) (pink lines). (e) and (f) The difference, $\Delta\rho_{yx}$, between ρ_{yx} and fits to Eq. (4) and Eq. (5), respectively.

regime, σ_{xy}^A is roughly independent of σ_{xx} , or $\sigma_{xy}^A \sim \text{constant}$ [48] and $\rho_{yx}^A = S'_H M \rho_{xx}^2$ [41]. In the bad-metal regime, $\sigma_{xx} < 10^4 (\Omega \text{ cm})^{-1}$, $\sigma_{yx}^A \propto \sigma_{xx}^n$, where $n \sim 1.6$ [48,61]. All samples studied in this work display large conductivities [$\sigma_{xx} > 10^4 (\Omega \text{ cm})^{-1}$]; therefore the remainder of this paper is concerned with the highly conductive and intrinsic regimes.

The third term in Eq. (1), $\Delta\rho_{yx}$, is the THE and is due to the nonzero SSC generated by noncoplanar spin textures. Such a contribution has been observed in both trivial noncoplanar spin textures [62,63], as well as topological spin textures [5,39,47,56].

To parse out the different contributions to the Hall effect in $\text{Eu}(\text{Ga}_{1-x}\text{Al}_x)_4$, two different methods are used. The first method is valid when $\rho_{yx} \ll \rho_{xx}$ and assumes a single dominant carrier type. This method is applicable where both

topological Hall and anomalous Hall contributions to ρ_{yx} are expected, and when $\rho_{yx}(H > H_c)$ is linear. Here, Eq. (1) can be written as

$$\rho_{yx} = R_0 \mu_0 H + S_H \rho_{xx} M + \Delta\rho_{yx}, \quad (2)$$

assuming skew scattering as the dominant scattering mechanism, or

$$\rho_{yx} = R_0 \mu_0 H + S'_H \rho_{xx}^2 M + \Delta\rho_{yx}, \quad (3)$$

assuming the intrinsic KL-type scattering mechanism [48].

For fields greater than $\mu_0 H_c$, $\Delta\rho_{yx}$ is necessarily zero since all spins are aligned in the SP state, and Eqs. (2) and (3) become

$$\frac{\rho_{yx}}{\mu_0 H} = R_0 + S_H \frac{\rho_{xx} M}{\mu_0 H} \quad (4)$$

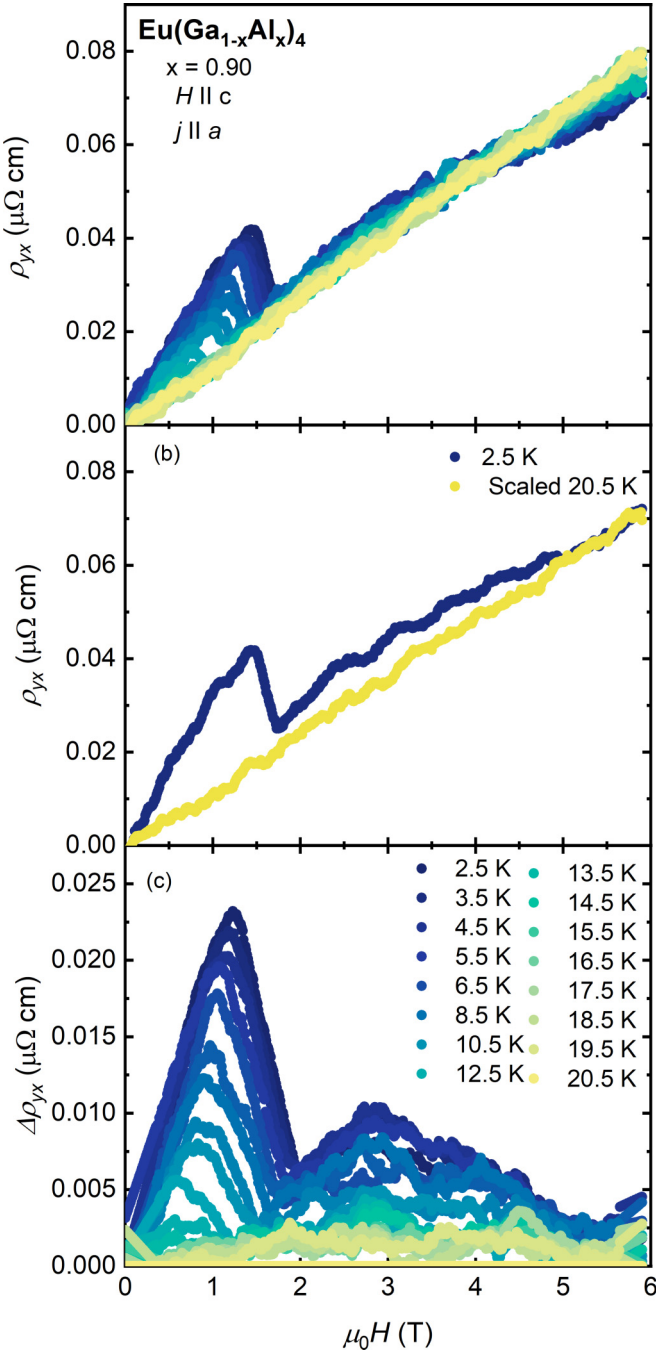


FIG. 3. (a) The Hall resistivity ρ_{yx} measured with magnetic field $H \parallel c$ and current $j \parallel a$ for fields $0\text{ T} \leq \mu_0H \leq 6\text{ T}$ and temperatures $2.5\text{ K} \leq T \leq 20.5\text{ K}$ for $\text{Eu}(\text{Ga}_{1-x}\text{Al}_x)_4$, $x = 0.90$. (b) ρ_{yx} at $T = 2.5\text{ K}$ (blue symbols) and ρ_{yx} at $T = 20.5\text{ K}$ (yellow symbols) scaled to the high-field regime of the $T = 2.5\text{ K}$ data. (c) The difference between the lower-temperature ρ_{yx} and scaled $T = 20.5\text{ K}$ data, $\Delta\rho_{yx}$, for $2.5\text{ K} \leq T \leq 19.5\text{ K}$.

and

$$\frac{\rho_{yx}}{\mu_0H} = R_0 + S'_H \frac{\rho_{xx}^2 M}{\mu_0H}, \quad (5)$$

respectively. R_0 and S_H or S'_H can thus be extracted as the intercept and slope of the corresponding line generated by

plotting ρ_{yx}/μ_0H vs $\rho_{xx}M/\mu_0H$ or vs ρ_{xx}^2M/μ_0H . $\Delta\rho_{yx}$ is then estimated below μ_0H_c as the difference

$$\Delta\rho_{yx} = \rho_{yx} - R_0\mu_0H - \rho_{yx}^A. \quad (6)$$

This analysis is demonstrated in Fig. 2 for $\text{Eu}(\text{Ga}_{1-x}\text{Al}_x)_4$ with $x = 0.71$, where the temperature dependence of $M(H)$, $\rho_{xx}(H)$, and $\rho_{yx}(H)$ is shown for $H \parallel c$ and $j \parallel a$ [panels (a)–(c)]. Fits of $\rho_{yx}(H)$ at $T = 2.5\text{ K}$ (blue) and $T = 20.5\text{ K}$ (yellow) to Eq. (4) (cyan line) and Eq. (5) (pink line) are presented in Fig. 2(d). For $T = 2.5\text{ K}$, both equations capture the behavior of $\rho_{yx}(H)$ for $H > H_c$, while for $H < H_c$, there are clear deviations of the measured $\rho_{yx}(H)$ compared to the fits, indicating an additional contribution $\Delta\rho_{yx}$. When $T = 20.5\text{ K}$, both equations capture all features of $\rho_{yx}(H)$ such that $\Delta\rho_{yx} = 0$.

The temperature and field dependence of $\Delta\rho_{yx}$ obtained after subtracting the normal and anomalous contributions from the measured ρ_{yx} [Eq. (6)] are shown in Figs. 2(e) and 2(f) evaluated from fits to Eqs. (4) and (5), respectively. Qualitatively, both methods for estimating $\Delta\rho_{yx}$ result in similar temperature and field dependencies. However, Eq. (5) does a slightly better job of minimizing $\Delta\rho_{yx}$, consistent with Ref. [27]. A similar analysis was done for $\text{Eu}(\text{Ga}_{1-x}\text{Al}_x)_4$ for $x = 0.50$ and 0.58 (shown in the Supplemental Material [64]).

This method works for $x = 0.50, 0.58$, and 0.71 . However, a different method needs to be used to evaluate the THE for $x = 0.90$ because ρ_{yx} above μ_0H_c shows a nonlinear field dependence (Fig. 3) for this composition, which requires a multiband description for the normal Hall effect, instead of a single-band analysis.

To extract $\Delta\rho_{yx}$ for $\text{Eu}(\text{Ga}_{1-x}\text{Al}_x)_4$ with $x = 0.90$, we follow the procedure done in Ref. [35]. Assuming there is only a weak temperature dependence of R_0 and ρ_{yx}^A , the scaled ρ_{yx} above T_N is used to extract the THE at low temperatures. Here, the $T = 20.5\text{ K}$ ($20.5\text{ K} > T_N$) data are scaled to the lower-temperature data, such that the high-field data collapse onto each other. Figure 3(b) shows this analysis where the $T = 20.5\text{ K}$ ρ_{yx} data (yellow) have been scaled to the $T = 2.5\text{ K}$ ρ_{yx} data (blue). $\Delta\rho_{yx}$ shown in Fig. 3(c) for all measured T is obtained by subtracting the scaled high temperature from the lower-temperature data, showing a clear THE. Such treatment precludes the analysis of ρ_{yx}^A .

As a result of this analysis, a contour map of $\Delta\rho_{yx}$ is produced, shown in Figs. 4(a)–4(d) for $\text{Eu}(\text{Ga}_{1-x}\text{Al}_x)_4$ with $x = 0.50, 0.58, 0.71$, and 0.90 . The H - T phase diagrams determined from isothermal magnetization (blue squares) and temperature-dependent magnetic susceptibility measurements (purple hexagons) [17,27] are shown together with the contour plots.

Overall, nonzero $\Delta\rho_{yx}$ can be observed in certain phase regions for all four compositions. For $x = 0.5$ [Fig. 4(a)], both the H - T phase diagram and $\Delta\rho_{yx}$ map are consistent with previous results [27]. Here, the AFM1 phase for $H = 0$ was determined to be a spin-density wave state with the magnetic moments perpendicular to the magnetic propagation vector q_{mag} along the crystallographic a axis [65]. The ground state, AFM3, was determined to be a cycloidal state again with q_{mag} along the crystallographic a axis, but with moments rotating in the ab plane [65]. The phase AFM2 that separates AFM1

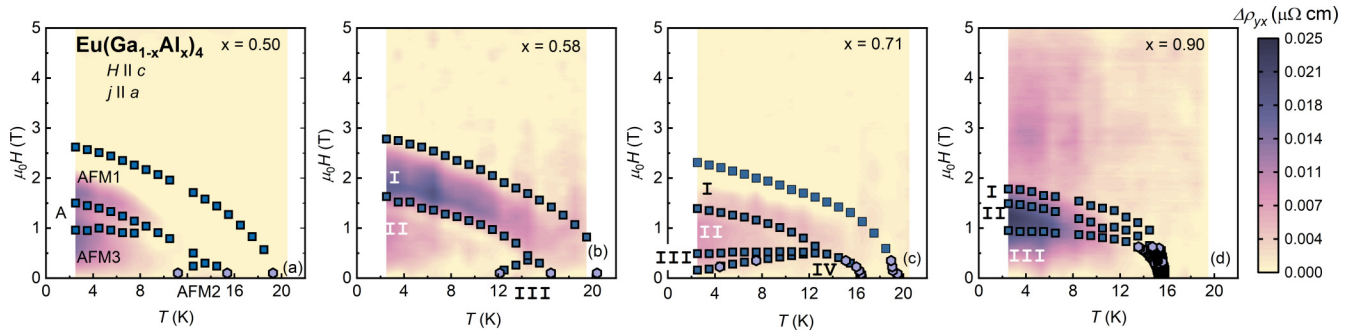


FIG. 4. Magnetic field–temperature (H - T) phase diagrams with magnetic field $H \parallel c$ for $\text{Eu}(\text{Ga}_{1-x}\text{Al}_x)_4$, (a) $x = 0.50$, (b) $x = 0.58$, (c) $x = 0.71$, and (d) $x = 0.90$. Blue squares are determined from maxima in dM/dH while purple hexagons are determined from $d(MT)/dT$. The color of the contour maps corresponds to the contribution to the topological Hall resistivity $\Delta\rho_{yx}$.

and AFM3 on cooling was determined to have mixed magnetic propagation vectors. With the application of magnetic field $H \parallel c$, AFM3 and AFM1 are separated by the intermediate field phase (A phase), where $\Delta\rho_{yx}$ is centered around, indicative of a topological spin texture or a more generic non-coplanar spin texture.

For $\text{Eu}(\text{Ga}_{1-x}\text{Al}_x)_4$ with $x = 0.58$, 0.71 , and 0.90 [Figs. 4(b)–4(d)], the maximum THE appears in the regions I, II, and II, respectively. We note that, for compositions $x = 0.50$, 0.58 , 0.71 , there is a double-peak feature in the signal Supplemental Material [64], and Figs. 2(e) and 2(f) that follows the phase boundaries. One explanation is that two different noncoplanar spin textures exist in these systems, as was also the case in EuAl_4 [22]. Another possibility is phase coexistence coming from two neighboring first-order transitions. Indeed, in $\text{Gd}_3\text{Ru}_4\text{Al}_{12}$ the THE has a double-peak feature, with the maxima on the phase boundaries where the skyrmion lattice is stabilized [56]. Further magnetic scattering experiments will be needed to elucidate such details in $\text{Eu}(\text{Ga}_{1-x}\text{Al}_x)_4$.

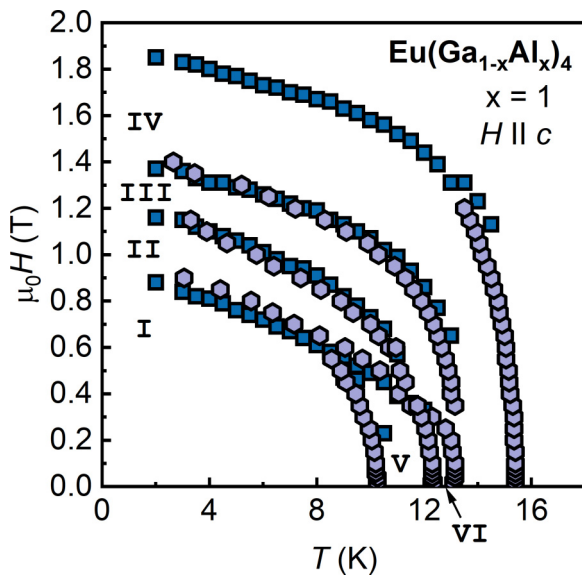


FIG. 5. Magnetic field–temperature phase diagram of EuAl_4 [$\text{Eu}(\text{Ga}_{1-x}\text{Al}_x)_4$, $x = 1$] for $H \parallel c$. The phase boundaries are determined by maxima in dM/dH (blue squares) and $d(MT)/dT$ (purple hexagons).

Next, we focus on $\text{Eu}(\text{Ga}_{1-x}\text{Al}_x)_4$ with $x = 0.9$, the compound closest in composition to the confirmed skyrmion host EuAl_4 [22]. Despite the existence of the THE in both compounds (the THE in EuAl_4 was reported in Ref. [23]), the phase diagrams are strikingly different. For comparison,

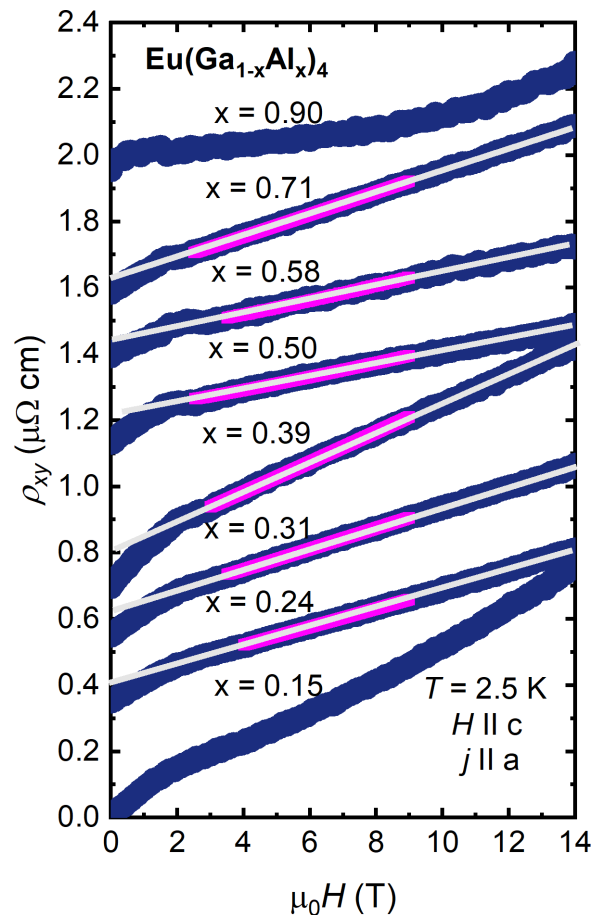


FIG. 6. Magnetic field dependence of the Hall resistivity ρ_{yx} (blue symbols) for $\text{Eu}(\text{Ga}_{1-x}\text{Al}_x)_4$ ($x = 0.15, 0.24, 0.31, 0.39, 0.50, 0.58, 0.71, 0.90$) measured at $T = 2.5$ K with $H \parallel c$ and $j \parallel a$ for $0 \text{ T} \leq \mu_0 H \leq 14 \text{ T}$. Data are offset such that $\rho_{yx}(H = 0) = 0$. Pink lines are fits to Eq. (5) in the field-polarized state up to $\mu_0 H = 9 \text{ T}$, the highest field we are able to measure magnetization. The gray lines are linear extrapolations of the pink lines.

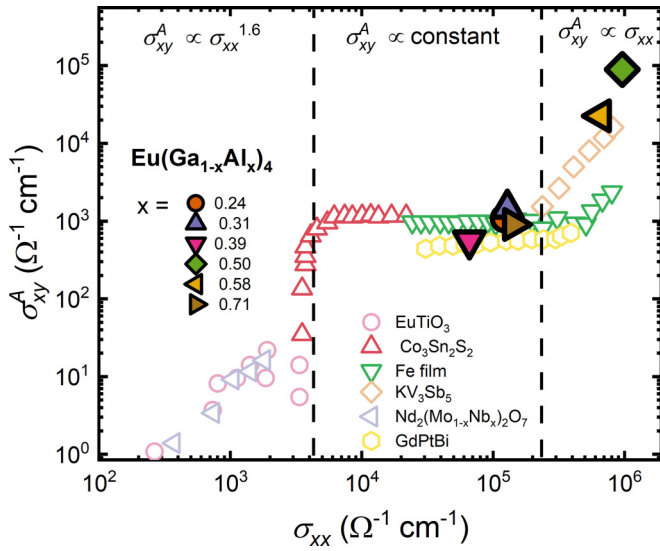


FIG. 7. The anomalous Hall conductivity σ_{xy}^A plotted as a function of longitudinal conductivity σ_{xx} for $\text{Eu}(\text{Ga}_{1-x}\text{Al}_x)_4$, $x = 0.24, 0.31, 0.39, 0.50, 0.58,$ and 0.71 , extracted from the field-polarized regime ($\mu_0 H = 9$ T) at temperature $T = 2.5$ K with fits to Eq. (5) (large, closed symbols) compared to other metallic magnets (small, open symbols) taken from Refs. [35–37,74–76].

the H - T phase diagram ($H \parallel c$) determined by magnetization measurements for EuAl_4 is presented in Fig. 5 which is consistent with previous reports [22]. EuAl_4 possesses four different magnetically ordered phases on zero-field cooling, labeled IV, VI, V, and I in Fig. 5. This is in contrast to $\text{Eu}(\text{Ga}_{1-x}\text{Al}_x)_4$ with $x = 0.9$, which only has two phases below T_N , labeled I and III in Fig. 4(d). Also, with the application of magnetic field $H \parallel c$, the zero-field phases in EuAl_4 (Fig. 5) are separated by two additional phases, phases II (rhombic skyrmion lattice) and III (square skyrmion lattice) [22], compared to only one intermediate field state in $\text{Eu}(\text{Ga}_{1-x}\text{Al}_x)_4$, $x = 0.9$ [phase II in Fig. 4(d)] where the THE reaches a maximum. The different H - T phase diagrams reflect the ability to fine-tune the magnetic interactions in the two compounds

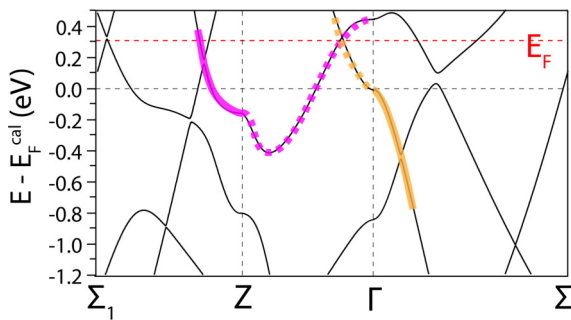


FIG. 8. The electronic structure calculated along certain high-symmetry lines for $\text{Eu}(\text{Ga}_{1-x}\text{Al}_x)_4$, $x = 0.5$, corresponding to the ordered structure EuGa_2Al_2 , in the paramagnetic state. The yellow and magenta lines mark out the bands that form a Dirac point. The red dashed line indicates the Fermi level determined by the ARPES experiments [77].

using chemical substitution, possibly favoring one type of skyrmion lattice over the other.

The Dzyaloshinskii-Moriya (DM) interaction [66,67] has been emphasized as a key ingredient in stabilizing topological spin textures in noncentrosymmetric crystals. However, the $\text{Eu}(\text{Ga}_{1-x}\text{Al}_x)_4$ crystal structure is centrosymmetric and therefore DM interactions should be absent [5]. Instead, recent theoretical studies [19,68–70] suggested that the interplay between the Ruderman-Kittel-Kasuya-Yosida (RKKY) interaction [71–73] and the four-spin interaction could stabilize topological spin-textures in metallic centrosymmetric magnets. In these theories [19,68–70], the RKKY interaction stabilizes q_{mag} set by the Fermi surface nesting vector, while the four-spin interaction, which depends on the in-plane bond-dependent anisotropy and easy-axis anisotropy, increases the propensity towards multi- q order. Being able to tune these interactions in centrosymmetric compounds offers the opportunity for tunable topological spin textures, which is in contrast to their noncentrosymmetric counterparts, where the type of topological spin texture is set by the crystalline symmetry [5]. Future experimental and theoretical works on $\text{Eu}(\text{Ga}_{1-x}\text{Al}_x)_4$ will elucidate the influence of chemical substitution on these tuning parameters, which may, in turn, enable targeted engineering of topological spin textures.

B. Anomalous Hall effect (AHE)

We now turn to the AHE in the SP state above H_c (where M is fully saturated at $T = 2.5$ K). Extended measurements of $\rho_{yx}(H)$, $\rho_{xx}(H)$, and $M(H)$ up to $\mu_0 H = 9$ T are shown in the Supplemental Material [64]. Equation (5) is used to extract the anomalous Hall resistivity as $\rho_{yx}^A = S_H' \frac{\rho_{xx}^2 M}{\mu_0 H}$. Such an analysis is valid only for the single-band Hall effect so the analysis is restricted to $\text{Eu}(\text{Ga}_{1-x}\text{Al}_x)_4$ with $0.24 \leq x \leq 0.71$. Fits to the $T = 2.5$ K data are shown in Fig. 6 as pink lines for $\mu_0 H_c \leq \mu_0 H \leq 9$ T. Next, ρ_{yx}^A is converted to anomalous Hall conductivity σ_{xy}^A using the tensor relation $\sigma_{xy}^A = \rho_{yx}^A / (\rho_{xx}^2 + \rho_{yx}^2)$. In Fig. 7, $\sigma_{xy}^A(\mu_0 H = 9$ T, $T = 2.5$ K) is plotted for each composition compared to $\sigma_{xx}(H = 0, T = 2.5$ K), which serves as a measure of disorder and naturally varies with x .

For $x = 0.24, 0.31, 0.39,$ and 0.71 , σ_{xy}^A is nearly independent of σ_{xx} , consistent with the intrinsic KL mechanism. The resulting $\sigma_{xy}^A = 600\text{--}1000$ ($\Omega \text{ cm})^{-1}$ is also comparable with the theoretical limit of $10^2 \sim 10^3$ ($\Omega \text{ cm})^{-1}$ when σ_{xy}^A is generated by reciprocal space Berry curvature [40]. The compounds with $x = 0.50$ and 0.58 are much more conductive, entering the regime where σ_{xy}^A is dominated by the skew-scattering mechanism. For these compositions, σ_{xy}^A increases with increasing σ_{xx} , which appears to be in line with the skew scattering mechanism. However, the Hall angle $\Theta_H = \tan^{-1}(\sigma_{xy}^A / \sigma_{xx})$ of typical metals where skew scattering dominates is usually less than 1% [40]. Θ_H measured for $\text{Eu}(\text{Ga}_{1-x}\text{Al}_x)_4$ with $x = 0.50$ is $\sim 7\%$ indicating that another mechanism (possibly intrinsic KL) is also contributing to the large σ_{xy}^A , a consequence of reciprocal-space Berry curvature.

The temperature dependence of σ_{xy}^A is often used to distinguish between the intrinsic and extrinsic mechanisms of the AHE [48]. σ_{xy}^A is expected to be nearly temperature inde-

pendent (dependent) in the intrinsic (extrinsic) regime. Such an analysis is only reliable when the coefficient R_0 (i.e., the carrier concentration) is temperature independent [41]. For $\text{Eu}(\text{Ga}_{1-x}\text{Al}_x)_4$, we find R_0 is temperature dependent, and therefore such an analysis is inconclusive.

First-principles calculations are used to further study the topological electronic structure, which is the origin of the reciprocal-space Berry curvature for the $\text{Eu}(\text{Ga}_{1-x}\text{Al}_x)_4$ series. The band structure of EuGa_2Al_2 in the paramagnetic state obtained by density functional theory (DFT) calculations is presented in Fig. 8, which shows a Dirac point along the Γ -Z path. The Dirac point is protected by the fourfold rotational symmetry with respect to the z axis in this tetragonal system: the two bands highlighted with magenta and yellow lines have different irreducible representations of the C_{4v} point group and cross each other along Γ -Z without opening a gap when spin-orbit coupling is considered. Note that this type of Dirac crossing is sometimes also called semi-Dirac or anisotropic Dirac crossing because the band dispersion is linear along one axis (k_z), while being quadratic along other axes (k_x and k_y). Such a crossing has been discussed in the study on the nonmagnetic isostructural analog BaAl_4 [78]. However, the Dirac crossing is located ~ 0.4 eV above the Fermi level in BaAl_4 .

The existence of the Dirac point in EuGa_2Al_2 is verified by ARPES measurements [77]. In the Brillouin zone (BZ) Z plane, there is a hole band (yellow dashed line) and an electron band (magenta dashed line) which intersect each other around the BZ center. The ARPES measurements [77] agree well with the DFT calculations and confirm the existence of the Dirac point along the Γ -Z path. More importantly, the Dirac point in EuGa_2Al_2 is found to be located close to the Fermi level by angle-resolved photoemission spectroscopy measurements [77], in contrast to the case of BaAl_4 [78]. In the SP state, the spin degeneracy of the bands will be lifted, which could lead to the formation of Weyl points. The mechanism is similar to that of GdPtBi [79–81], where the gapless quadratic band touching in the electronic structure sets the stage for the field-induced Weyl physics and the AHE.

Finally, it is noted that the energy of the Dirac point in the $\text{Eu}(\text{Ga}_{1-x}\text{Al}_x)_4$ series may slightly vary as the Al/Ga ratio changes. In EuGa_4 , for example, the Dirac point was determined to be above the Fermi level [18] in contrast to EuGa_2Al_2 . Possible reasons for the changing Fermi surface, which affect both the transport and magnetic properties in $\text{Eu}(\text{Ga}_{1-x}\text{Al}_x)_4$, include chemical doping, chemical pressure, or disorder, which are inherent to chemical substitution. Since Ga and Al are isovalent, chemical doping is not likely. In $\text{Eu}(\text{Ga}_{1-x}\text{Al}_x)_4$, chemical pressure would be expected with Al-Ga substitution, since the Ga atomic radius r_{Ga} is 15%–20% larger than r_{Al} [82]. However, the lattice parameters of the end compounds in this series EuAl_4 and EuGa_4 are virtually identical [17], which suggests very little unit cell

variation across the series. On the other hand, a change in the in-plane lattice spacing a with x in $\text{Eu}(\text{Ga}_{1-x}\text{Al}_x)_4$ has been reported [17], which indicates a minimum in a and unit cell volume at the ordered composition $x = 0.5$. Even with this nonmonotonic change, the overall variation in unit cell volume is only $\sim 6\%$.

The disorder effects are comparable across all doped samples since their absolute $\rho(T)$ and residual resistivity ratios RRR are comparable [17], while the disorder effects are minimized near the ordered compositions. Overall, the variation of transport and magnetic properties observed in $\text{Eu}(\text{Ga}_{1-x}\text{Al}_x)_4$ can be interpreted as a convolution of chemical pressure and disorder.

IV. CONCLUSIONS

In conclusion, magnetotransport measurements on $\text{Eu}(\text{Ga}_{1-x}\text{Al}_x)_4$ single crystals with $0.15 \leq x \leq 0.9$ reveal evidence of a THE for $x \geq 0.5$, pointing to the existence of noncoplanar spin textures. For intermediate composition $0.24 < x < 0.39$, the Hall resistivity varies smoothly with magnetic field, although multiple magnetic ordered phases are clearly revealed in the isothermal magnetization and longitudinal resistivity measurements. Our measurements suggest a weak THE contribution, if any of the phase regimes host topological spin textures. At the lowest doping $x = 0.15$, only one magnetic ordered phase can be observed before reaching the SP state, similar to the end compound EuGa_4 . Therefore, no topological spin texture is expected. In the SP state, evidence of a large AHE in $\text{Eu}(\text{Ga}_{1-x}\text{Al}_x)_4$ is found, which is attributed to the appearance of Weyl nodes, generated after spin splitting of a Dirac point. The existence of the Dirac point near the Fermi level in the paramagnetic state in EuGa_2Al_2 is confirmed by DFT calculations which has been verified by ARPES measurements. Therefore $\text{Eu}(\text{Ga}_{1-x}\text{Al}_x)_4$ for $x \geq 0.5$ is established as a rare platform to study the field-tunable phenomena associated with reciprocal- and real-space topology.

ACKNOWLEDGMENTS

Y.G., S.L., and E.M. acknowledge partial support from AFOSR Grant No. FA9550-21-1-0343. J.M.M. has been supported by the NSF Graduate Research Fellowship Program under Grant No. DGE-1842494 and National Science Foundation (NSF) DMR Grant No. 1903741. K.A. and E.M. have been partially supported by the Robert A. Welch Foundation Grant No. C-2114. The use of the EPMA facility at the Department of Earth Science, Rice University, Houston, Texas, is kindly acknowledged. The authors thank Gelu Costin for help with EPMA measurements. J.H. and M.Y. acknowledge support from the Gordon and Betty Moore Foundation's EPiQS Initiative through Grant No. GBMF9470 and the Robert A. Welch Foundation Grant No. C-2175.

- [1] F. D. M. Haldane, *Phys. Rev. Lett.* **61**, 2015 (1988).
 [2] C.-X. Liu, S.-C. Zhang, and X.-L. Qi, *Annu. Rev. Condens. Matter Phys.* **7**, 301 (2016).

- [3] M. V. Berry, *Proc. R. Soc. London, Ser. A* **392**, 45 (1984).
 [4] C.-Z. Chang, J. Zhang, X. Feng, J. Shen, Z. Zhang, M. Guo, K. Li, Y. Ou, P. Wei, L.-L. Wang *et al.*, *Science* **340**, 167 (2013).

- [5] Y. Tokura and N. Kanazawa, *Chem. Rev.* **121**, 2857 (2021).
- [6] A. Fert, V. Cros, and J. Sampaio, *Nat. Nanotechnol.* **8**, 152 (2013).
- [7] A. Fert, N. Reyren, and V. Cros, *Nat. Rev. Mater.* **2**, 17031 (2017).
- [8] K. M. Song, J.-S. Jeong, B. Pan, X. Zhang, J. Xia, S. Cha, T.-E. Park, K. Kim, S. Finizio, J. Raabe *et al.*, *Nat. Electron.* **3**, 148 (2020).
- [9] F. Jonietz, S. Mühlbauer, C. Pfleiderer, A. Neubauer, W. Münzer, A. Bauer, T. Adams, R. Georgii, P. Böni, R. A. Duine *et al.*, *Science* **330**, 1648 (2010).
- [10] N. Nagaosa and Y. Tokura, *Nat. Nanotechnol.* **8**, 899 (2013).
- [11] W. Jiang, G. Chen, K. Liu, J. Zang, S. G. Te Velthuis, and A. Hoffmann, *Phys. Rep.* **704**, 1 (2017).
- [12] J. Jiang, D. Xiao, F. Wang, J.-H. Shin, D. Andreoli, J. Zhang, R. Xiao, Y.-F. Zhao, M. Kayyalha, L. Zhang *et al.*, *Nat. Mater.* **19**, 732 (2020).
- [13] Y. Li, S. Xu, J. Wang, C. Wang, B. Yang, H. Lin, W. Duan, and B. Huang, *Proc. Natl. Acad. Sci. USA* **119**, e2122952119 (2022).
- [14] P. Li, J. Ding, S. S.-L. Zhang, J. Kally, T. Pillsbury, O. G. Heinonen, G. Rimal, C. Bi, A. DeMann, S. B. Field *et al.*, *Nano Lett.* **21**, 84 (2021).
- [15] W.-J. Zou, M.-X. Guo, J.-F. Wong, Z.-P. Huang, J.-M. Chia, W.-N. Chen, S.-X. Wang, K.-Y. Lin, L. B. Young, Y.-H. G. Lin *et al.*, *ACS Nano* **16**, 2369 (2022).
- [16] R. Xiao, D. Xiao, J. Jiang, J.-H. Shin, F. Wang, Y.-F. Zhao, R.-X. Zhang, A. Richardella, K. Wang, M. Kayyalha *et al.*, *Phys. Rev. Res.* **3**, L032004 (2021).
- [17] M. Stavinoha, J. A. Cooley, S. G. Minasian, T. M. McQueen, S. M. Kauzlarich, C.-L. Huang, and E. Morosan, *Phys. Rev. B* **97**, 195146 (2018).
- [18] S. Lei, K. Allen, J. Huang, J. M. Moya, B. Casas, Y. Zhang, M. Hashimoto, D. Lu, J. Denlinger, L. Balicas *et al.*, [arXiv:2208.06407](https://arxiv.org/abs/2208.06407).
- [19] S. Hayami, R. Ozawa, and Y. Motome, *Phys. Rev. B* **95**, 224424 (2017).
- [20] T. Kawasaki, K. Kaneko, A. Nakamura, N. Aso, M. Hedo, T. Nakama, T. Ohhara, R. Kiyonagi, K. Oikawa, I. Tamura *et al.*, *J. Phys. Soc. Jpn.* **85**, 114711 (2016).
- [21] H. Zhang, X. Zhu, Y. Xu, D. Gawryluk, W. Xie, S. Ju, M. Shi, T. Shiroka, Q. Zhan, E. Pomjakushina *et al.*, *J. Phys.: Condens. Matter* **34**, 034005 (2022).
- [22] R. Takagi, N. Matsuyama, V. Ukleev, L. Yu, J. S. White, S. Francoual, J. R. Mardegan, S. Hayami, H. Saito, K. Kaneko *et al.*, *Nat. Commun.* **13**, 1472 (2022).
- [23] T. Shang, Y. Xu, D. Gawryluk, J. Ma, T. Shiroka, M. Shi, and E. Pomjakushina, *Phys. Rev. B* **103**, L020405 (2021).
- [24] W. R. Meier, J. R. Torres, R. P. Hermann, J. Zhao, B. Lavina, B. C. Sales, and A. F. May, *Phys. Rev. B* **106**, 094421 (2022).
- [25] K. Kaneko, T. Kawasaki, A. Nakamura, K. Munakata, A. Nakao, T. Hanashima, R. Kiyonagi, T. Ohhara, M. Hedo, T. Nakama *et al.*, *J. Phys. Soc. Jpn.* **90**, 064704 (2021).
- [26] S. Shimomura, H. Murao, S. Tsutsui, H. Nakao, A. Nakamura, M. Hedo, T. Nakama, and Y. Ōnuki, *J. Phys. Soc. Jpn.* **88**, 014602 (2019).
- [27] J. M. Moya, S. Lei, E. M. Clements, C. S. Kengle, S. Sun, K. Allen, Q. Li, Y. Peng, A. A. Husain, M. Mitrano *et al.*, *Phys. Rev. Mater.* **6**, 074201 (2022).
- [28] J. Rodríguez-Carvajal, *Phys. B: Condens. Matter* **192**, 55 (1993).
- [29] G. Kresse and J. Furthmüller, *Phys. Rev. B* **54**, 11169 (1996).
- [30] J. P. Perdew, K. Burke, and M. Ernzerhof, *Phys. Rev. Lett.* **77**, 3865 (1996).
- [31] A. A. Mostofi, J. R. Yates, Y.-S. Lee, I. Souza, D. Vanderbilt, and N. Marzari, *Comput. Phys. Commun.* **178**, 685 (2008).
- [32] M. L. Sancho, J. L. Sancho, and J. Rubio, *J. Phys. F* **14**, 1205 (1984).
- [33] M. L. Sancho, J. L. Sancho, J. L. Sancho, and J. Rubio, *J. Phys. F* **15**, 851 (1985).
- [34] L. Ye, M. Kang, J. Liu, F. Von Cube, C. R. Wicker, T. Suzuki, C. Jozwiak, A. Bostwick, E. Rotenberg, D. C. Bell *et al.*, *Nature (London)* **555**, 638 (2018).
- [35] T. Suzuki, R. Chisnell, A. Devarakonda, Y.-T. Liu, W. Feng, D. Xiao, J. W. Lynn, and J. Checkelsky, *Nat. Phys.* **12**, 1119 (2016).
- [36] E. Liu, Y. Sun, N. Kumar, L. Muechler, A. Sun, L. Jiao, S.-Y. Yang, D. Liu, A. Liang, Q. Xu *et al.*, *Nat. Phys.* **14**, 1125 (2018).
- [37] S.-Y. Yang, Y. Wang, B. R. Ortiz, D. Liu, J. Gayles, E. Derunova, R. Gonzalez-Hernandez, L. Šmejkal, Y. Chen, S. S. Parkin *et al.*, *Sci. Adv.* **6**, eabb6003 (2020).
- [38] A. K. Nayak, J. E. Fischer, Y. Sun, B. Yan, J. Karel, A. C. Komarek, C. Shekhar, N. Kumar, W. Schnelle, J. Kübler *et al.*, *Sci. Adv.* **2**, e1501870 (2016).
- [39] T. Kurumaji, T. Nakajima, M. Hirschberger, A. Kikkawa, Y. Yamasaki, H. Sagayama, H. Nakao, Y. Taguchi, T.-h. Arima, and Y. Tokura, *Science* **365**, 914 (2019).
- [40] Y. Fujishiro, N. Kanazawa, R. Kurihara, H. Ishizuka, T. Hori, F. S. Yasin, X. Yu, A. Tsukazaki, M. Ichikawa, M. Kawasaki *et al.*, *Nat. Commun.* **12**, 317 (2021).
- [41] M. Lee, Y. Onose, Y. Tokura, and N. P. Ong, *Phys. Rev. B* **75**, 172403 (2007).
- [42] S. Liang, J. Lin, S. Kushwaha, J. Xing, N. Ni, R. J. Cava, and N. P. Ong, *Phys. Rev. X* **8**, 031002 (2018).
- [43] R. Singha, S. Roy, A. Pariari, B. Satpati, and P. Mandal, *Phys. Rev. B* **99**, 035110 (2019).
- [44] J. Chen, H. Li, B. Ding, H. Zhang, E. Liu, and W. Wang, *Appl. Phys. Lett.* **118**, 031901 (2021).
- [45] O. Pavlosiuk, P. Fałat, D. Kaczorowski, and P. Wiśniewski, *APL Mater.* **8**, 111107 (2020).
- [46] Y. Zhu, B. Singh, Y. Wang, C.-Y. Huang, W.-C. Chiu, B. Wang, D. Graf, Y. Zhang, H. Lin, J. Sun, A. Bansil, and Z. Mao, *Phys. Rev. B* **101**, 161105(R) (2020).
- [47] M. Lee, W. Kang, Y. Onose, Y. Tokura, and N. P. Ong, *Phys. Rev. Lett.* **102**, 186601 (2009).
- [48] N. Nagaosa, J. Sinova, S. Onoda, A. H. MacDonald, and N. P. Ong, *Rev. Mod. Phys.* **82**, 1539 (2010).
- [49] D. Xiao, M.-C. Chang, and Q. Niu, *Rev. Mod. Phys.* **82**, 1959 (2010).
- [50] R. Karplus and J. Luttinger, *Phys. Rev.* **95**, 1154 (1954).
- [51] K. Ohgushi, S. Murakami, and N. Nagaosa, *Phys. Rev. B* **62**, R6065 (2000).
- [52] R. Shindou and N. Nagaosa, *Phys. Rev. Lett.* **87**, 116801 (2001).
- [53] I. Martin and C. Batista, *Phys. Rev. Lett.* **101**, 156402 (2008).
- [54] D. J. Thouless, M. Kohmoto, M. P. Nightingale, and M. den Nijs, *Phys. Rev. Lett.* **49**, 405 (1982).
- [55] F. D. M. Haldane, *Phys. Rev. Lett.* **93**, 206602 (2004).

- [56] M. Hirschberger, T. Nakajima, S. Gao, L. Peng, A. Kikkawa, T. Kurumaji, M. Kriener, Y. Yamasaki, H. Sagayama, H. Nakao *et al.*, *Nat. Commun.* **10**, 5831 (2019).
- [57] A. Nakamura, Y. Hiranaka, M. Hedo, T. Nakama, Y. Tatetsu, T. Maehira, Y. Miura, A. Mori, H. Tsutsumi, Y. Hirose *et al.*, *J. Phys. Soc. Jpn.* **82**, 124708 (2013).
- [58] H. Chen, Q. Niu, and A. H. MacDonald, *Phys. Rev. Lett.* **112**, 017205 (2014).
- [59] A. Neubauer, C. Pfleiderer, B. Binz, A. Rosch, R. Ritz, P. G. Niklowitz, and P. Böni, *Phys. Rev. Lett.* **102**, 186602 (2009).
- [60] N. D. Khanh, T. Nakajima, X. Yu, S. Gao, K. Shibata, M. Hirschberger, Y. Yamasaki, H. Sagayama, H. Nakao, L. Peng *et al.*, *Nat. Nanotechnol.* **15**, 444 (2020).
- [61] S. Onoda, N. Sugimoto, and N. Nagaosa, *Phys. Rev. Lett.* **97**, 126602 (2006).
- [62] Q. Wang, K. J. Neubauer, C. Duan, Q. Yin, S. Fujitsu, H. Hosono, F. Ye, R. Zhang, S. Chi, K. Krycka *et al.*, *Phys. Rev. B* **103**, 014416 (2021).
- [63] N. J. Ghimire, R. L. Dally, L. Poudel, D. Jones, D. Michel, N. T. Magar, M. Bleuel, M. A. McGuire, J. Jiang, J. Mitchell *et al.*, *Sci. Adv.* **6**, eabe2680 (2020).
- [64] See Supplemental Material at <http://link.aps.org/supplemental/10.1103/PhysRevB.108.064436> for extended measurements.
- [65] A. Vibhakar, D. Khalyavin, J. Moya, P. Manuel, F. Orlandi, S. Lei, E. Morosan, and A. Bombardi, [arXiv:2304.07903](https://arxiv.org/abs/2304.07903).
- [66] I. Dzyaloshinsky, *J. Phys. Chem. Solids* **4**, 241 (1958).
- [67] T. Moriya, *Phys. Rev. Lett.* **4**, 228 (1960).
- [68] R. Ozawa, S. Hayami, and Y. Motome, *Phys. Rev. Lett.* **118**, 147205 (2017).
- [69] Z. Wang, Y. Su, S.-Z. Lin, and C. D. Batista, *Phys. Rev. Lett.* **124**, 207201 (2020).
- [70] S. Hayami and Y. Motome, *Phys. Rev. B* **103**, 024439 (2021).
- [71] M. A. Ruderman and C. Kittel, *Phys. Rev.* **96**, 99 (1954).
- [72] T. Kasuya, *Prog. Theor. Phys.* **16**, 45 (1956).
- [73] K. Yosida, *Phys. Rev.* **106**, 893 (1957).
- [74] K. S. Takahashi, H. Ishizuka, T. Murata, Q. Y. Wang, Y. Tokura, N. Nagaosa, and M. Kawasaki, *Sci. Adv.* **4**, eaar7880 (2018).
- [75] T. Miyasato, N. Abe, T. Fujii, A. Asamitsu, S. Onoda, Y. Onose, N. Nagaosa, and Y. Tokura, *Phys. Rev. Lett.* **99**, 086602 (2007).
- [76] S. Iguchi, N. Hanasaki, and Y. Tokura, *Phys. Rev. Lett.* **99**, 077202 (2007).
- [77] J. Moya *et al.* (to be published).
- [78] K. Wang, R. Mori, Z. Wang, L. Wang, J. H. S. Ma, D. W. Latzke, D. E. Graf, J. D. Denlinger, D. Campbell, B. A. Bernevig *et al.*, [arXiv:2007.12571](https://arxiv.org/abs/2007.12571).
- [79] M. Hirschberger, S. Kushwaha, Z. Wang, Q. Gibson, S. Liang, C. A. Belvin, B. A. Bernevig, R. J. Cava, and N. P. Ong, *Nat. Mater.* **15**, 1161 (2016).
- [80] C. Shekhar, N. Kumar, V. Grinenko, S. Singh, R. Sarkar, H. Luetkens, S.-C. Wu, Y. Zhang, A. C. Komarek, E. Kampert *et al.*, *Proc. Natl. Acad. Sci. USA* **115**, 9140 (2018).
- [81] J. Cano, B. Bradlyn, Z. Wang, M. Hirschberger, N. P. Ong, and B. A. Bernevig, *Phys. Rev. B* **95**, 161306(R) (2017).
- [82] R. D. Shannon, *Acta. Cryst. A* **32**, 751 (1976).